Asymmetric instability in thin-film flow down a fiber

Chase T. Gabbard and Joshua B. Bostwick*
Department of Mechanical Engineering, Clemson University, Clemson, South Carolina 29631, USA

(Received 11 November 2020; accepted 11 March 2021; published 29 March 2021)

Thin-film flow down a vertical fiber gives rise to a number of instabilities that define the bead-on-fiber morphology including Plateau-Rayleigh breakup, isolated bead formation, and convective instabilities. Experiments are performed that reveal an asymmetric instability which depends upon the liquid surface tension and fiber diameter and exhibits all the bead-on-fiber morphologies. The bead dynamics are described by the bead spacing and bead velocity, with the asymmetric morphology displaying more regular dynamics than the symmetric morphology. For the asymmetric morphology, the transition from the Plateau-Rayleigh to convective regime agrees well with predictions for a free viscous jet, indicating a minimal effect between the thin film and fiber. In addition, the dimensionless bead velocity is shown to scale with the capillary number for all experimental data. These observations for the asymmetric bead dynamics can be used as a design tool for heat and mass transfer applications.

DOI: 10.1103/PhysRevFluids.6.034005

I. INTRODUCTION

Thin-film flow down fibers can cause shape-change instabilities resulting in the bead-on-fiber morphology with associated high surface area-to-volume ratios that are desirable in applications where heat and mass transfer across a liquid-gas interface occurs, such as gas absorption [1–3], heat exchangers [4,5], microfluidics [6], and desalination [7]. These beading patterns are driven by surface tension and are the result of the well-known Plateau-Rayleigh hydrodynamic instability (PRI) [8,9]. Recent research involving PRI includes investigations into nonlinear effects, the role of viscosity on the breakup time [10], the stability of liquid bridges [11,12], and the role of liquid-solid contact [13]. In this paper, we perform an experimental investigation of thin-film flow down fibers and report an asymmetric beading instability and its dependence upon the liquid surface tension and fiber diameter.

A thin liquid film coating a fiber similarly experiences PRI, but a nontrivial base flow generates a more complex set of instabilities, including the emergence of a convective instability resulting in both steady and unsteady temporal beading patterns. Kliakhandler *et al.* [14] performed experiments and documented the three primary regimes: isolated, Plateau-Rayleigh, and convective. Recent work by Sadeghpour *et al.* [15] and Ji *et al.* [16] has examined the affect of nozzle size on the observed regime. Interestingly, it is seen that when the flow rate and fiber size are held constant, all three regimes are observable simply by altering the nozzle diameter. Experiments performed by Smolka *et al.* [17] explored the effects of altering the fluid properties and Haefner *et al.* [18] analyzed the influence of slip on the Plateau-Rayleigh instability on a fiber, showing that the hydrodynamic boundary conditions at the solid-liquid interface do not affect the dominating wavelength but do affect the growth rate of the undulations.

*jbostwi@clemson.edu; https://cecas.clemson.edu/~jbostwi/

Volume effects on thin-film flows are also important and Quéré [19] showed the conditions for which drops cease to form and how it depends upon the film thickness and fiber diameter. Using scaling arguments presented by Frenkel [20], Kalliadasis and Chang [21] found solitary wave solutions using a matched asymptotic analysis and determined a critical thickness h_c, which must be exceeded for beads to develop. Chang and Demekhin [22] further studied thin fluid films and showed that for $h > h_c$, where h_c is the critical thickness, fluid films evolve into continually growing pulses and become convectively unstable. Several proposed models, including a weakly nonlinear thin-film model by Craster and Matar [23] and the creeping-flow, thick-film model proposed by Kliakhandler *et al.* [14], have shown partial agreement with experiments but lead to slight discrepancies and an inability to accurately predict the emergence of the convective regime. Several other models have been developed in an attempt to reconcile these discrepancies by considering slip-enhanced drop formation [24], different scalings [25], streamwise viscous diffusion [26], and disjoining pressure effects [27]. A more comprehensive review of the models used to describe these thin-film flows is found in [28].

A single drop placed on a fiber can spread into a film or can morph into either an asymmetric or symmetric drop profile based on which is energetically preferred [29]. The transition of a symmetric drop profile to one which is asymmetric has been extensively studied [30–34] and is referred to as the "roll-up process." Investigations into this process have highlighted the importance of both the volume and surface tension of the liquid drop on the transition between profile symmetries. Likewise, one would expect a similar dependence in thin-film flow down fibers with the fluid inertia influencing the transition point. We report an experimental observation documenting the emergence of this instability.

We perform experiments in thin-film flows down fibers, documenting the emergence of an asymmetric instability and showing its critical dependence on fiber diameter D_f and surface tension σ. The bead dynamics are characterized by the bead velocity V_b and spacing S_b and we contrast the dynamics for symmetric and asymmetric bead morphologies. The point where the flow regime transitions from the Plateau-Rayleigh to convective regime is important and we show that the transition point for the asymmetric morphology is more predictable, which is advantageous in heat and mass transfer applications. These results can be used to improve novel water desalination processes as described in the concluding remarks, which are critical in addressing global issues that will continue to shape and define the next century of scientific endeavors [7].

II. EXPERIMENT

Beading patterns were investigated using the experimental setup shown in Fig. 1(a). Liquid is pumped by a NE-1000 syringe pump at flow rate Q through a stainless-steel nozzle of diameter D_n onto a nylon fiber of diameter D_f. The range of Q explored is 5–650 mL/hr, D_n is 0.4–3.3 mm, and D_f is 0.101–0.5080 mm. Two pinning devices are located at the top and bottom of the testing apparatus and hold the fiber in a vertical orientation. The length of the fiber is 550 mm, which is sufficient for the beading patterns to become fully developed.

Three working liquids are used: (i) glycerol-water mixtures, (ii) silicone oil, and (iii) mineral oil, with the liquid properties given in Table I. These liquids were selected to provide a large range of viscosity and surface tension values. A surfactant was added to the glycerol-water mixtures to change the surface tension, while the volume fraction of glycerol to water changes the viscosity of the mixture. The density ρ, viscosity μ, and surface tension σ of each used liquid are determined using an Anton Paar DMA 35 density meter, Anton Paar MCR 302 rheometer, and a Kruss K100 surface tensiometer with Wilhelmy plate, respectively.

The bead dynamics were recorded using a camera at 960 frames per second. MATLAB is used for image processing to analyze the experiments. The beading pattern dynamics can be defined by the bead velocity V_b, bead spacing S_b, and bead diameter D_b, as shown in Fig. 1(b). Each of these properties are measured at a significant distance down the fiber such that nozzle effects are no longer observable and the pattern has become fully developed. It is worth noting that since asymmetric

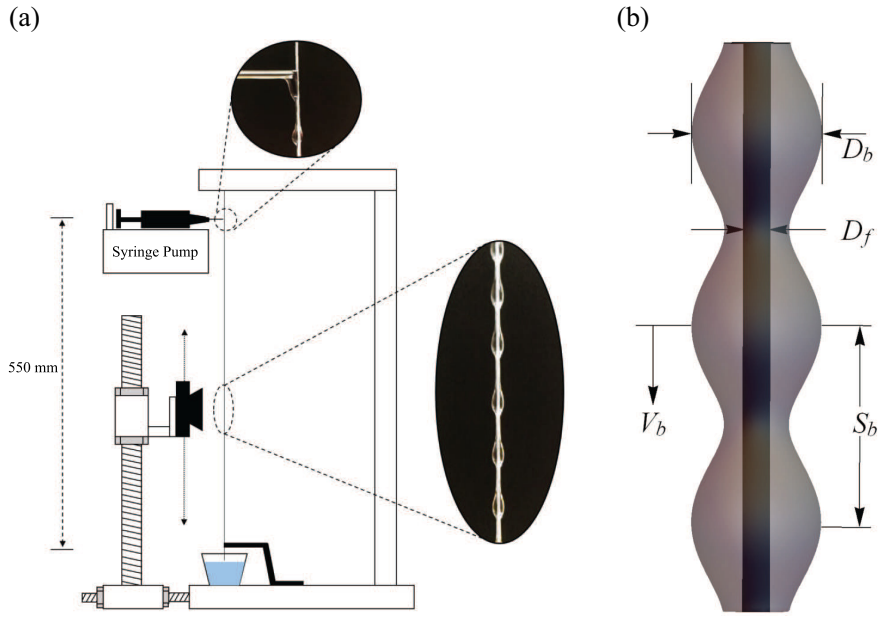

FIG. 1. (a) Experimental setup and (b) sketch of the bead properties showing the bead spacing S_b, bead velocity V_b, bead diameter D_b, and fiber diameter D_f.

beading patterns allow beads to rotate about the fiber, exact values for the bead diameter are much harder to attain and, for this reason, we do not analyze bead diameters for asymmetric bead profiles. Three bead patterns are observed: (i) isolated, (ii) Plateau-Rayleigh, and (iii) convective, consistent with prior results [14]. These three regimes are shown in Fig. 3, where the isolated and Plateau-Rayleigh regimes both exhibit a regular bead pattern with primary beads moving with constant velocity and spacing. However, the isolated regime experiences a secondary breakup of the thin liquid column between the primary beads which leads to smaller, secondary beads. The convective regime is characterized by irregular bead patterns that result in random coalescence events between primary beads. We focus on the isolated and Plateau-Rayleigh regimes, where the beading patterns are steady and repeatable in experiment. In the convective regime, bead patterns have properties that vary significantly from moment to moment due to coalescence events occurring at irregular distances down the fiber.

Lastly, we scale our data and plot against several dimensionless numbers to provide insight into the physics. The Reynolds number Re is defined as $\mathrm{Re} = \rho Q D_f / A\mu$, where the characteristic length is the fiber diameter used in the experiment, A is the cross-sectional area of the nozzle, and Q is the volumetric flow rate. The Reynolds number gives a comparison of inertial to viscous forces and the use of the fiber diameter as the characteristic length allows scaling relationships that also account for the fiber geometry. The capillary number Ca is defined as $\mathrm{Ca} = \mu Q / A\sigma$ and provides a comparison

TABLE I. Liquid properties.

Fluid	Density ρ (kg/m^3)	Viscosity μ (mPa s)	Surface tension σ (mN/m)
Glycerol-water	1040–1243	85–787	30–60
Silicone oil	936–974	9.4–974	22
Mineral oil	848	17.3	25

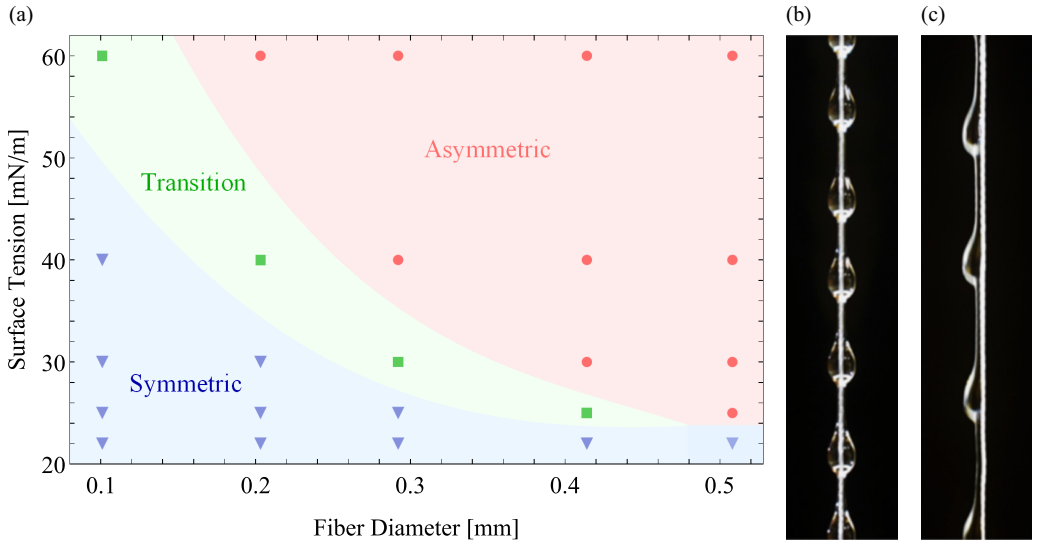

FIG. 2. (a) Phase diagram of the bead symmetry, as it depends upon the surface tension and fiber diameter for the observed (b) symmetric and (c) asymmetric morphology.

between the viscous and capillary forces. We define a nondimensional bead velocity $V^* = V_b/V_n$ as the ratio of bead velocity to nozzle velocity, $V_n = Q/A$. Lastly, for experiments performed at the transition point between absolute and convective instability, we define a nondimensional transition velocity $\tilde{V} = V_b/(\sigma/3\mu)$, where V_b is scaled by the velocity $U_0^{A/C} = \sigma/3\mu$ at the transition between absolute and convective instability for a free viscous jet [35].

III. RESULTS AND DISCUSSION

Experimental data have been collected, from which we observe an asymmetric instability in the bead morphology. Our focus is on (i) the symmetric-asymmetric transition and (ii) characterizing the associated bead dynamics over a large range of experimental parameters. We show that asymmetric beading exhibits more predictable dynamics, similar to that of a free viscous jet, as measured at the transition from the Plateau-Rayleigh to convective regime. Furthermore, the nondimensional bead velocity V^* for all asymmetric patterns collapses upon scaling with the capillary number. Herein, error bars correspond to two standard deviations.

A. Symmetry transition

Figure 2(a) plots the observed bead symmetry for the full range of fiber diameters and surface tensions shown in Table I, with typical experimental images of the symmetric [Fig. 2(b)] and asymmetric [Fig. 2(c)] morphology. Here, the viscosity μ, flow rate Q, and nozzle diameter D_n are observed to each play a minimal role in determining the final symmetry of the flow and thus the data points that are shown are approximately invariant to each of these experimental variables. Interestingly, there exists a narrow range of values where the bead profile struggles to reach a final configuration and transitions from symmetric to asymmetric morphologies in a random fashion. Herein, we present data that clearly display symmetric or asymmetric morphology. Note, in Fig. 2(a), the dependence of the bead symmetry on fiber diameter and surface tension. We observe that (i) for fixed fiber diameter, the transition from symmetric to asymmetric occurs as surface tension increases, and (ii) for fixed surface tension, the transition from symmetric to asymmetric occurs as the fiber diameter increases. These results agree with intuition, as we expect,

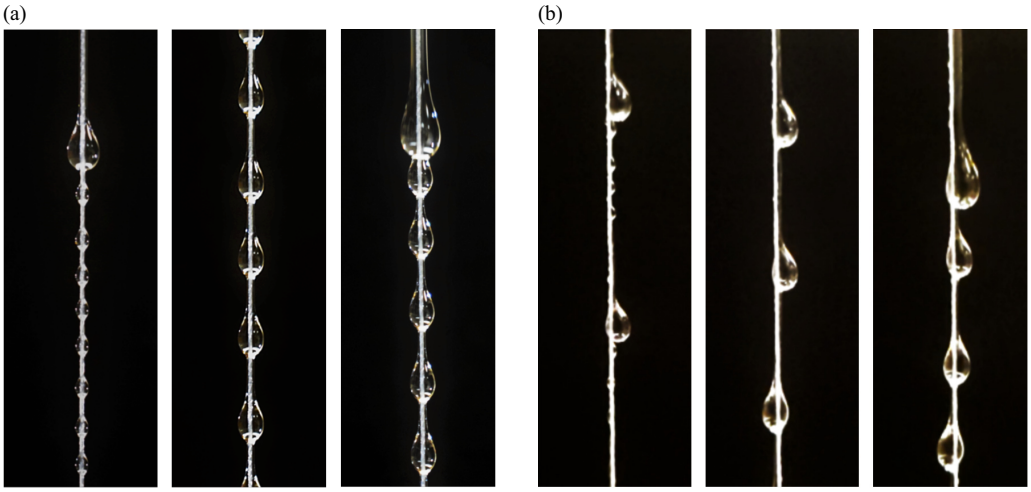

FIG. 3. (a) Symmetric and (b) asymmetric bead morphology exhibit isolated (left), Plateau-Rayleigh (middle), and convective (right) regimes. The bead diameters shown in the middle image of (a) and (b) are 2.38 and 2.245 mm, respectively.

for vanishingly small fiber diameters, only a symmetric morphology to occur, consistent with the Plateau-Rayleigh instability of a liquid column.

No symmetry-breaking transition is observed when changing other experimental parameters. Changing the nozzle diameter significantly affects the flow regime developed for both the asymmetric and symmetric morphology, but no effect on the flow symmetry is observed. Changing the viscosity affects the timescale of the symmetry transition, but not the final state. This is readily observed when comparing various viscosity silicone oils and observing the transition to a symmetric morphology occurring at different locations along the fiber. Low-viscosity silicone oils quickly transition to the symmetric state, whereas high-viscosity silicone oils transition more slowly. Pinching the fiber during an asymmetric flow obstructs the liquid flow and we observe a quick buildup of liquid above the pinched point that causes the flow to wrap the fiber into a symmetric configuration. Releasing the fiber allows the now symmetric morphology to flow freely, and a quick transition back to the asymmetric configuration is observed. Lastly, we mention that a small set of experiments was performed with a 3-meter-long fiber to demonstrate that no symmetry transitions occur and our 550 mm fiber length is sufficient to characterize the bead morphology and dynamics.

B. Beading regime

Kliakhandler *et al.* [14] categorized fully developed symmetric beading patterns into three primary regimes: isolated, Plateau-Rayleigh, and convective. We observe these same three primary regimes for both the symmetric and asymmetric morphology, as shown in Fig. 3. The isolated regime, shown in the left images in Figs. 3(a) and 3(b), is characterized by equally spaced primary beads moving at a constant velocity that are separated by smaller secondary beads. Note that both primary and secondary beads display the same morphology, either symmetric or asymmetric. The Plateau-Rayleigh regime, shown in the middle images of Figs. 3(a) and 3(b), results in primary beads which flow down the fiber with equal spacing and velocity. However, unlike the isolated regime, the Plateau-Rayleigh regime is characterized by the absence of the secondary beads separating the primary beads. Here, the thin film separating the primary beads does not have time for the secondary Plateau-Rayleigh instability to develop. Lastly, the convective regime illustrated in the far-right images of Figs. 3(a) and 3(b) is characterized by the coalescence of primary beads into larger, dominant beads, which progress down the fiber with increasing volume and velocity as they

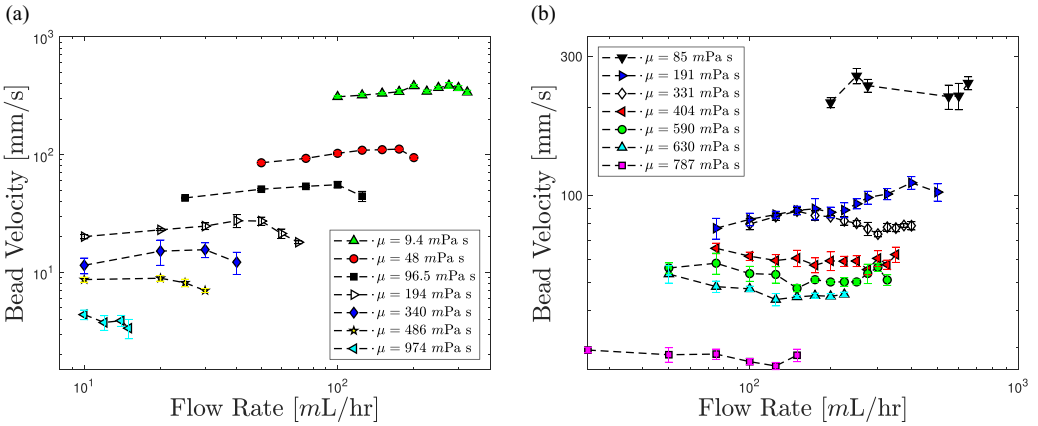

FIG. 4. Bead velocity V_b against flow rate Q, as it depends upon viscosity μ for the (a) symmetric and (b) asymmetric morphology for a fixed nozzle diameter $D_n = 1.2$ mm and fiber diameter $D_f = 0.2032$ mm.

coalesce with the smaller primary beads. Interestingly, we observe bead rotation about the axis of the fiber for the asymmetric morphology and note that the average angular velocity of the beads tends to increase with decreasing viscosity. The physical mechanism for this rotation has not been investigated here.

The flow regime is influenced by each experimental parameter. The flow-rate effects are best illustrated in Fig. 3, where flow rate increases from left to right in each subfigure. The isolated regime is observed at low flow rates and increasing the flow rate results in a transition to the Plateau-Rayleigh regime, with further increases leading to the convective regime. The effect of the fiber diameter is similar to that described for the flow rate, where increases to the fiber diameter will result in transitions from the isolated to Plateau-Rayleigh to convective regime. Unlike fiber diameter and flow rate, the role of the nozzle diameter on the regime is much more complex and several investigations have already explored this effect [15,16].

The transition between the regimes is often difficult to determine experimentally, especially between the Plateau-Rayleigh and convective regimes. This is best observed by increasing the flow rate until the point where the steady primary bead pattern observed in the Plateau-Rayleigh regime exhibits its first coalescence event, at which point the convective regime is entered. We note that the majority of applications which utilize these beading patterns benefit from maximal surface area-to-volume ratios. This occurs in the Plateau-Rayleigh regime and is optimized just below the transition to the convective regime, as the curvature increases with flow rate up until this point. Once the convective regime is reached, coalescence events create large dominant beads, which move with increasing velocity down the fiber, clearing out all previously existing primary beads, and ultimately yield no benefit compared to the Plateau-Rayleigh regime. Accordingly, we are particularly interested in this transition point and discuss relevant applications in the concluding remarks.

C. Quantifying the beading properties

Figure 4 plots the bead velocity V_b against the flow rate Q, showing that increased viscosity leads to decreased bead velocity, as could be expected. For similar viscosity liquids, the bead velocity for the asymmetric morphology is much higher than for the symmetric morphology. This is due to the smaller interaction between the liquid and fiber and associated reduction in viscous dissipation. In Fig. 4, for each data set, the point with the highest flow rate corresponds to the boundary between the Plateau-Rayleigh and convective regimes. We now focus on this transition point. A stark contrast between the two morphologies is seen in Fig. 5, where the bead spacing S_b against

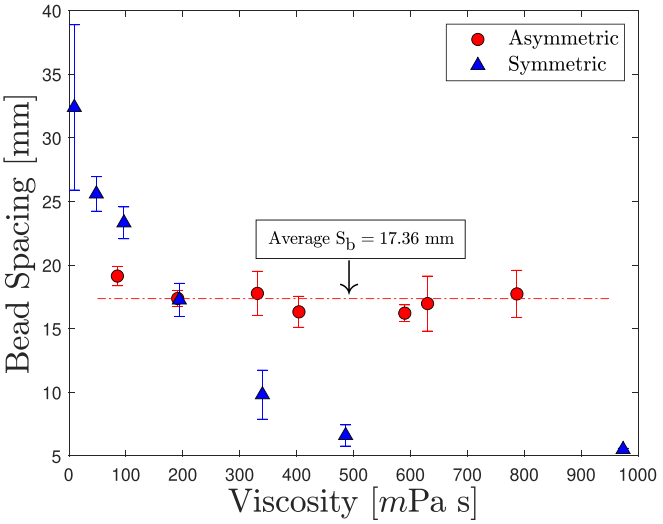

FIG. 5. Bead spacing S_b against viscosity μ at the onset of the convective regime for nozzle diameter $D_n = 1.2$ mm and fiber diameter $D_f = 0.2032$ mm.

the viscosity μ is plotted for only transition points. Contrasting the two symmetries, we see a large variation in the bead spacing for the symmetric morphologies and a near-constant bead spacing for the asymmetric morphologies. The average bead spacing for the asymmetric morphology is approximately 17.36 mm for this set of experimental conditions. The significant difference in behavior at the transition shown in Fig. 5 motivates us to further explore the differences between the two morphologies at their transition point.

The transition point between the Plateau-Rayleigh and convective regimes occurs at the point when the flow transitions from absolutely to convectively unstable. We motivate our data analysis by stating results from the literature for the bead-on-fiber geometry and free viscous jet. For the bead-on-fiber geometry, Duprat *et al.* [36], Duclaux *et al.* [37] derived the dispersion relationship,

$$\omega = kU_0 + i\frac{\sigma h_0^3}{3\mu R_f^4}[(kR_f)^2 - (kR_f)^4], \tag{1}$$

where ω is the frequency, k is the wave number, h_0 is the film thickness, and U_0 is the base flow velocity. The transition from absolute to convective instability is determined by locating the saddle point k_0 of the dispersion relationship, which yields the critical velocity at transition,

$$U_0^{A/C} = 1.62\frac{\sigma h_0^3}{3\mu R_f^3}. \tag{2}$$

We hypothesize that the behavior of the asymmetric morphology, which is inherently less affected by the fiber, will behave similarly to a free viscous jet. To draw a physical comparison between the two, we consider the dispersion relationship for a free viscous jet as derived by Eggers and Dupont [35],

$$\omega = kU_0 + i\frac{\sigma}{6\mu R_0}[1 - (kR_0)^2], \tag{3}$$

where R_0 is the initial radius of the jet. We again locate the saddle point k_0 of the dispersion relationship and determine the velocity at transition to be

$$U_0^{A/C} = \frac{1}{3}\frac{\sigma}{\mu}. \tag{4}$$

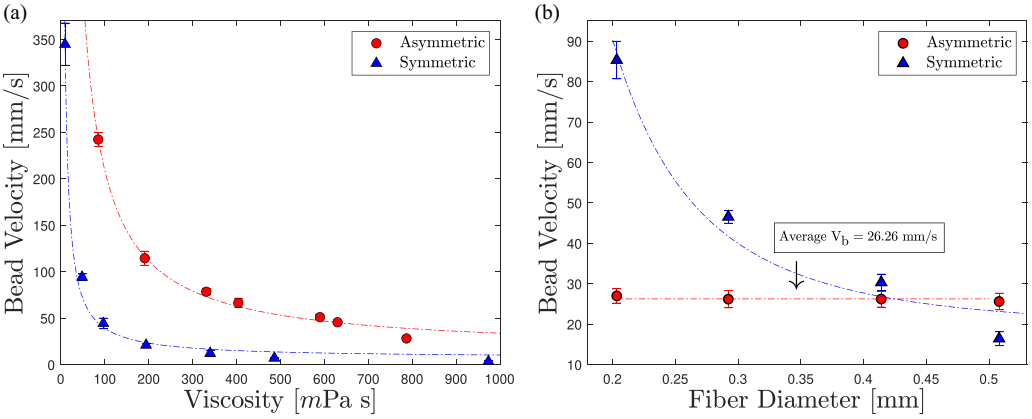

FIG. 6. (a) Bead velocity against viscosity at the onset of the convective regime for nozzle diameter $D_n = 1.2$ mm and fiber diameter $D_f = 0.2032$ mm. (b) Bead velocity V_b against fiber diameter D_f at the onset of the convective regime contrasting the symmetric ($\mu = 48$ mPa s) and asymmetric ($\mu = 787$ mPa s) morphology for $D_n = 1.2$ mm.

The transition velocity $U_0^{A/C}$ now provides us with a means to analyze the similarities of the asymmetric morphology to that of the free jet.

Figure 6(a) plots the bead velocity against the viscosity at the onset of the convective regime, contrasting the asymmetric and symmetric morphology. Here we see that the bead velocity rapidly decreases with increased viscosity for both morphologies, but the asymmetric velocity is always larger than the symmetric velocity for a fixed viscosity. The transition velocity for the bead-on-fiber, given by Eq. (2), and free viscous jet, given by Eq. (4), both exhibit a $1/\mu$ dependence, and we overlay Eq. (2) onto our symmetric data and Eq. (4) onto our asymmetric data in Fig. 6(a). This observation suggests that the asymmetric instability has physics governed by the free viscous jet with minimal effects due to the liquid-fiber interaction. Figure 6(b) plots the bead velocity against the fiber diameter at the onset of the convective regime, showing a significant decrease in velocity with increased fiber diameter for the symmetric morphology and a constant velocity 26.6 mm/s for the asymmetric morphology, irrespective of the fiber diameter. The dependence of the bead velocity on fiber diameter agrees well with Eq. (2) (blue dashed line) for the symmetric morphology and with Eq. (4) for the asymmetric morphology, which predicts a constant velocity $V_b \approx 25.4$ mm/s that is within 5% of the observed value (red dashed line).

Our results for the asymmetric morphology shown in Fig. 6 suggest a connection with the free viscous jet, which we theorize is a more general result that holds for all values of the experimental variables explored here. To investigate, we define a nondimensional transition velocity $\tilde{V} = V_b/(\sigma/3\mu)$, with $\tilde{V} \approx 1$ for flows similar to the free viscous jet. Figure 7 plots the transition velocity $\tilde{V}$ against Reynolds number Re for all of our data. The data are highly scattered for the symmetric morphologies. However, the asymmetric transition points show good agreement with the predicted transition velocity of a free jet and the average value $\tilde{V} = 1.061$.

D. Scaling the data

Earlier, we showed that the bead transition velocity closely followed that predicted by the theory for a viscous free jet (cf. Fig. 7). This observation along with the regularity of the asymmetric morphology suggests that we attempt to collapse all of our data upon scaling. Figure 8 plots the bead velocity ratio V^* against the capillary number Ca for all of our data, showing a reasonable collapse of the asymmetric data with power-law relationship $V^* \sim \mathrm{Ca}^{-0.8}$. Recall that the data presented in Fig. 8 were for the isolated or Plateau-Rayleigh regimes, where we observe $\mathrm{Ca} < 1$, suggesting

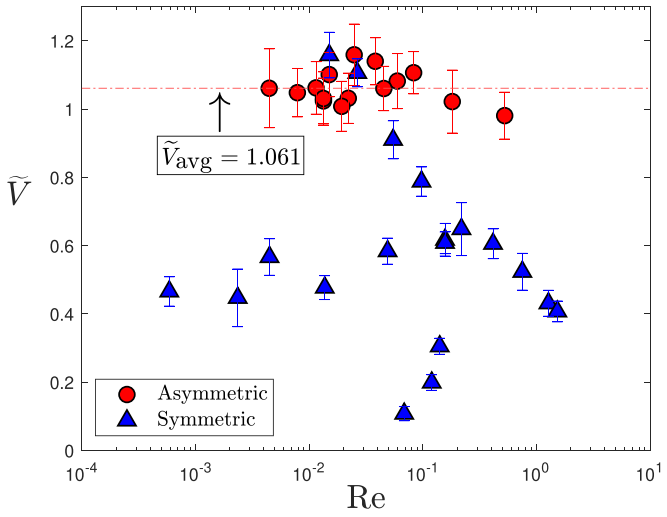

FIG. 7. Transition velocity ratio $\tilde{V}$ against Reynolds number Re at the absolute-convective transition point contrasting the symmetric and asymmetric morphology for all data.

that surface tension forces are dominant. This behavior again follows similarly to that predicted for a viscous free jet. We can quantitatively compare our data to theory for the free viscous jet by evaluating Eq. (3) at the maximum growth rate, $\gamma_{\max} = \mathrm{Im}[\omega] = (1/6)(\sigma/\mu R_0)$, and by defining the characteristic velocity as $V_{\mathrm{ch}} = \gamma_{\max} R_0 = (1/6)(\sigma/\mu)$. Letting $V^* = V_b/V_n \approx V_{\mathrm{ch}}/U_0^{A/C}$ yields $V^* = (1/6)\mathrm{Ca}^{-1}$. The dashed line in Fig. 8 shows a power-law fit $V^* \sim \mathrm{Ca}^{-1}$ to our data, further highlighting the similarities between the asymmetric morphology and a viscous free jet. Coupling this relationship with the earlier observation that $\tilde{V} \approx 1$ at the point of transition between absolute and convective instability, we see that the capillary number Ca and $\tilde{V}$ can be used as a design tool for many applications where the transition point to the convective regime is needed. For example, regular beading patterns are preferred in gas absorption [1,3], specifically in the Plateau-Rayleigh

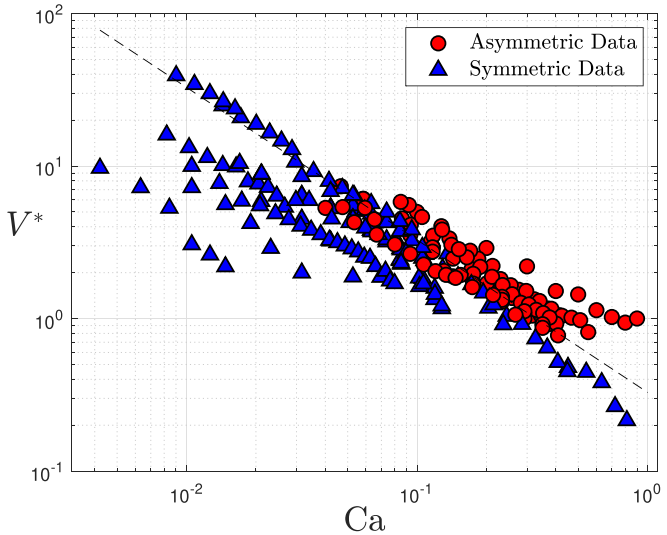

FIG. 8. Bead velocity ratio V^* against capillary number Ca for all data.

regime which exists just before irregular beading patterns emerge. The relationships that exist for the asymmetric morphology require only that the fluid properties be known in order to determine where the transition from the desired regular pattern to irregular ones will occur for a given flow rate. Thus, gas-absorption devices utilizing the asymmetric morphology can be designed for optimal performance.

IV. CONCLUSIONS

An experimental investigation into the bead morphologies that develop in the flow of thin liquid films down a fiber was performed. We report an experimental observation of an asymmetric instability and show how the symmetry of the instability depends upon the surface tension and fiber diameter. The instability morphology is independent of viscosity and flow rate. For both the symmetric and asymmetric morphology, three flow regimes are observed: isolated, Plateau-Rayleigh, and convective. We report how the bead velocity and bead spacing depend upon the experimental parameters in the isolated and Plateau-Rayleigh regimes. In general, the asymmetric morphology displays more predictable dynamics than the symmetric morphology. For example, the transition from Plateau-Rayleigh to convective regimes is important and we show that the bead velocity is nearly constant over a range of fiber diameters and the bead spacing is constant over a large range of viscosity for the asymmetric regime. The data for the symmetric morphology show much variability in these ranges. We show that the asymmetric morphology exhibits similar dynamics at the absolute-convective transition point to that of a free jet and that the transition velocity $\tilde{V}$ provides a reliable means for predicting this transition point in asymmetric flows. Lastly, we show that all asymmetric data collapse upon scaling the bead velocity ratio V^* with the capillary number Ca.

These observations provide insight into the underlying physics at play in thin-film flow down a fiber. Features of the asymmetric morphology exploited through our experimentation show trends and regularities that are advantageous for several application areas. The ability to accurately predict the point of transition between regimes is a key advantage of the asymmetric morphology for interfacial heat and mass transfer processes. For example, Sadeghpour *et al.* [7] presented a desalination process that utilizes thin-film flow down an array of fibers and showed that its optimal performance occurs for regular beading patterns with maximal bead frequency. These flows occur prior to the the transition between the Plateau-Rayleigh and convective regimes, which we have shown is both more robust and predictable for the asymmetric morphology. Thus, the asymmetric morphology can be taken advantage of for the design of optimal fluid patterns in this system that could provide a lightweight, economic option for clean-water production in resource-constrained communities around the globe. Although we have highlighted a few impactful applications, the breadth of applications and physics which describe this asymmetric instability remain highly untouched by the scientific community, and thus this work provides an initial investigation into a topic with many fruitful areas yet to be explored.

ACKNOWLEDGMENT

J.B.B. acknowledges support from NSF Grant No. CMMI-1935590.

APPENDIX: FREQUENCY TRENDS

The bead frequency $f = V_b/S_b$ is a critical property of thin-film flow down a fiber in determining the heat and mass transfer rates across the fluid interface. Increasing the bead frequency produces a higher total surface area in which mass and heat transfer can occur. In Figs. 5 and 6(b), we showed that the asymmetric morphology exhibits near-constant values of bead spacing and velocity at the transition between the Plateau-Rayleigh and convective regimes. Figure 9 plots the bead frequency f against the flow rate Q for all of our data, encompassing changes in viscosity, nozzle diameter, fiber diameter, and surface tension. As expected, a regularity emerges among the data for

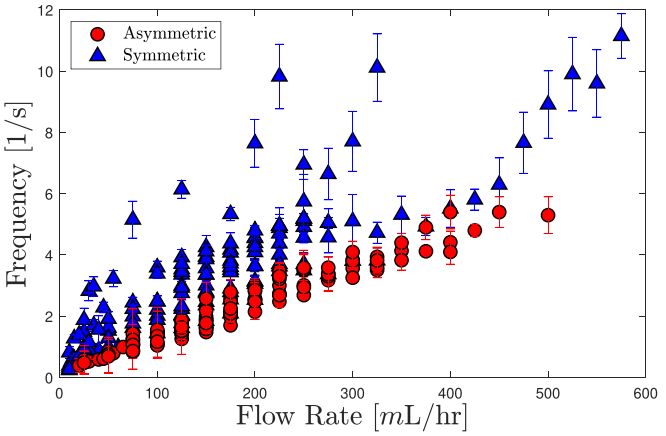

FIG. 9. Frequency f against flow rate Q for all data.

the asymmetric morphology, which is a drastic contrast from the large variance of the symmetric data. The frequency for asymmetric morphologies collapses to a trend line, which has powerful implications in applications where the frequency must be accurately predicted.

[1] S. M. Hosseini, R. Alizadeh, E. Fatehifar, and A. Alizadehdakhel, Simulation of gas absorption into string-of-beads liquid flow with chemical reaction, Heat Mass Transfer **50**, 1393 (2014).

[2] J. Grünig, E. Lyagin, S. Horn, T. Skale, and M. Kraume, Mass transfer characteristics of liquid films flowing down a vertical wire in a counter current gas flow, Chem. Eng. Sci. **69**, 329 (2012).

[3] H. Chinju, K. Uchiyama, and Y. H. Mori, "String-of-beads" flow of liquids on vertical wires for gas absorption, AIChE J. **46**, 937 (2000).

[4] Z. Zeng, A. Sadeghpour, G. Warrier, and Y. S. Ju, Experimental study of heat transfer between thin liquid films flowing down a vertical string in the Rayleigh-Plateau instability regime and a counterflowing gas stream, Intl. J. Heat Mass Transf. **108**, 830 (2017).

[5] Z. Zeng, A. Sadeghpour, and Y. S. Ju, Thermohydraulic characteristics of a multi-string direct-contact heat exchanger, Intl. J. Heat Mass Transf. **126**, 536 (2018).

[6] T. Gilet, D. Terwagne, and N. Vandewalle, Digital microfluidics on a wire, Appl. Phys. Lett. **95**, 014106 (2009).

[7] A. Sadeghpour, Z. Zeng, H. Ji, N. D. Ebrahimi, A. L. Bertozzi, and Y. S. Ju, Water vapor capturing using an array of traveling liquid beads for desalination and water treatment, Sci. Adv. **5**, eaav7662 (2019).

[8] J. A. F. Plateau, Experimental and theoretical researches on the figures on equilibrium of a liquid mass withdrawn from the action of gravity, *Annual Report of the Board of Regents of the Smithsonian Institution* (Government Printing Office, Washington, D.C., 1863), pp. 207–285.

[9] L. Rayleigh, On the instability of jets, Proc. London Math. Soc. **s1-10**, 4 (1878).

[10] A. Javadi, J. Eggers, D. Bonn, M. Habibi, and N. M. Ribe, Delayed Capillary Breakup of Falling Viscous Jets, Phys. Rev. Lett. **110**, 144501 (2013).

[11] B. J. Lowry and P. H. Steen, Capillary surfaces: Stability from families of equilibria with application to the liquid bridge, Proc. R. Soc. London, Ser. A: Math. Phys. Sci. **449**, 411 (1995).

[12] J. B. Bostwick and P. H. Steen, Liquid-bridge shape stability by energy bounding, IMA J. Appl. Math. **80**, 1759 (2015).

[13] J. B. Bostwick and P. H. Steen, Stability of constrained cylindrical interfaces and the torus lift of Plateau-Rayleigh, J. Fluid Mech. **647**, 201 (2010).

[14] I. L. Kliakhandler, S. H. Davis, and S. G. Bankoff, Viscous beads on vertical fibre, J. Fluid Mech. **429**, 381 (2001).
[15] A. Sadeghpour, Z. Zeng, and Y. S. Ju, Effects of nozzle geometry on the fluid dynamics of thin liquid films flowing down vertical strings in the Rayleigh-Plateau regime, Langmuir **33**, 6292 (2017).
[16] H. Ji, A. Sadeghpour, Y. S. Ju, and A. L. Bertozzi, Modeling film flows down a fibre influenced by nozzle geometry, arXiv:2007.09582.
[17] L. B. Smolka, J. North, and B. K. Guerra, Dynamics of free surface perturbations along an annular viscous film, Phys. Rev. E **77**, 036301 (2008).
[18] S. Haefner, M. Benzaquen, O. Bäumchen, T. Salez, R. Peters, J. D. McGraw, K. Jacobs, E. Raphaël, and K. Dalnoki-Veress, Influence of slip on the Plateau-Rayleigh instability on a fibre, Nat. Commun. **6**, 7409 (2015).
[19] D. Quéré, Thin films flowing on vertical fibers, Europhys. Lett. **13**, 721 (1990).
[20] A. L. Frenkel, Nonlinear theory of strongly undulating thin films flowing down vertical cylinders, Europhys. Lett. **18**, 583 (1992).
[21] S. Kalliadasis and H.-C. Chang, Drop formation during coating of vertical fibres, J. Fluid Mech. **261**, 135 (1994).
[22] H.-C. Chang and E. A. Demekhin, Mechanism for drop formation on a coated vertical fibre, J. Fluid Mech. **380**, 233 (1999).
[23] R. V. Craster and O. K. Matar, On viscous beads flowing down a vertical fibre, J. Fluid Mech. **553**, 85 (2006).
[24] D. Halpern and H.-H. Wei, Slip-enhanced drop formation in a liquid falling down a vertical fibre, J. Fluid Mech. **820**, 42 (2017).
[25] L. Yu and J. Hinch, The velocity of 'large' viscous drops falling on a coated vertical fibre, J. Fluid Mech. **737**, 232 (2013).
[26] C. Ruyer-Quil, S. P. M. J. Trevelyan, F. Giorgiutti-Dauphiné, C. Duprat, and S. Kalliadasis, Film flows down a fiber: Modeling and influence of streamwise viscous diffusion, Eur. Phys. J.: Spec. Top. **166**, 89 (2009).
[27] H. Ji, C. Falcon, A. Sadeghpour, Z. Zeng, Y. S. Ju, and A. L. Bertozzi, Dynamics of thin liquid films on vertical cylindrical fibers, arXiv:1901.00065.
[28] C. Ruyer-Quil and S. Kalliadasis, Wavy regimes of film flow down a fiber, Phys. Rev. E **85**, 046302 (2012).
[29] Françoise Brochard-Wyart, J.-M. Di Meglio, and D. Quéré, Theory of the dynamics of spreading of liquids on fibers, J. Phys. **51**, 293 (1990).
[30] B. J. Carroll, The equilibrium of liquid drops on smooth and rough circular cylinders, J. Colloid Interface Sci. **97**, 195 (1984).
[31] B. J. Carroll, Equilibrium conformations of liquid drops on thin cylinders under forces of capillarity. A theory for the roll-up process, Langmuir **2**, 248 (1986).
[32] G. McHale, S. M. Rowan, M. I. Newton, and N. A. Käb, Estimation of contact angles on fibers, J. Adhes. Sci. Technol. **13**, 1457 (1999).
[33] G. McHale, M. I. Newton, and B. J. Carroll, The shape and stability of small liquid drops on fibers, Oil Gas Sci. Technol. **56**, 47 (2001).
[34] G. McHale and M. I. Newton, Global geometry and the equilibrium shapes of liquid drops on fibers, Colloids Surf., A **206**, 79 (2002).
[35] J. Eggers and T. F. Dupont, Drop formation in a one-dimensional approximation of the Navier-Stokes equation, J. Fluid Mech. **262**, 205 (1994).
[36] C. Duprat, C. Ruyer-Quil, S. Kalliadasis, and F. Giorgiutti-Dauphiné, Absolute and Convective Instabilities of a Viscous Film Flowing Down a Vertical Fiber, Phys. Rev. Lett. **98**, 244502 (2007).
[37] V. Duclaux, C. Clanet, and D. Quéré, The effects of gravity on the capillary instability in tubes, J. Fluid Mech. **556**, 217 (2006).